

Differential interactions determine anisotropies at interfaces of RNA-based biomolecular condensates

Received: 17 September 2024

Accepted: 1 April 2025

Published online: 11 April 2025



Nadia A. Erkamp ^{1,2,3,11}, Mina Farag ^{2,4,11}, Yuanxin Qiu ^{2,5,11}, Daoyuan Qian ¹, Tomas Sneideris ¹, Tingting Wu⁵, Timothy J. Welsh¹, Hannes Ausserwöger ¹, Tommy J. Krug⁶, Gaurav Chauhan ^{2,4,10}, David A. Weitz ^{6,7,8}, Matthew D. Lew ^{2,5}  , Tuomas P. J. Knowles ^{1,9}  & Rohit V. Pappu ^{2,4} 

Biomolecular condensates form via macromolecular phase separation. Here, we report results from our characterization of synthetic condensates formed by phase separation of mixtures comprising two types of RNA molecules and the biocompatible polymer polyethylene glycol. Purine-rich RNAs are scaffolds that drive phase separation via heterotypic interactions. Conversely, pyrimidine-rich RNA molecules are adsorbents defined by weaker heterotypic interactions. They adsorb onto and wet the interfaces of coexisting phases formed by scaffolds. Lattice-based simulations reproduce the phenomenology observed in experiments and these simulations predict that scaffolds and adsorbents have different non-random orientational preferences at interfaces. Dynamics at interfaces were probed using single-molecule tracking of fluorogenic probes bound to RNA molecules. These experiments revealed dynamical anisotropy at interfaces whereby motions of probe molecules parallel to the interface are faster than motions perpendicular to the interface. Taken together, our findings have broad implications for designing synthetic condensates with tunable interfacial properties.

Biomolecular condensates are compositionally distinct membraneless bodies that form via phase separation of macromolecules^{1–3}. Condensates are two- or multi-phase systems that provide spatial and temporal control and organization over biochemical reactions involving proteins and nucleic acids^{1–5}. There is growing interest in developing synthetic condensates with bespoke functions^{6–11}. These efforts are being driven by advances in our understanding of the physico-

chemical principles underlying the formation and dissolution of condensates in live cells^{12–19} and in vitro^{14,15,19–23}. In live cells, condensates comprise several distinct types of macromolecules²⁴. Additionally, within dense phases of condensates, one often observes a hierarchical organization of the constituent macromolecules. This has been reported for stress granules^{18,25,26}, nucleoli^{15,27,28}, nuclear speckles²⁹, and the mitochondrial nucleoid⁵. Spatially organized condensates were also

¹Yusuf Hamied Department of Chemistry, Centre for Misfolding Disease, University of Cambridge, Cambridge, UK. ²Center for Biomolecular Condensates, James McKelvey School of Engineering, Washington University in St. Louis, St. Louis, MO, USA. ³Institute for Complex Molecular Systems (ICMS), Department of Biomedical Engineering, Eindhoven University of Technology, Eindhoven, The Netherlands. ⁴Department of Biomedical Engineering, James McKelvey School of Engineering, Washington University in St. Louis, St. Louis, MO, USA. ⁵Department of Electrical and Systems Engineering, James McKelvey School of Engineering, Washington University in St. Louis, St. Louis, MO, USA. ⁶John A. Paulson School of Engineering and Applied Sciences, Harvard University, Cambridge, MA, USA. ⁷Department of Physics, Harvard University, Cambridge, MA, USA. ⁸Wyss Institute for Biologically Inspired Engineering, Harvard University, Cambridge, MA, USA. ⁹Department of Physics, Cavendish Laboratory, University of Cambridge, Cambridge, UK. ¹⁰Present address: Department of Chemical Engineering, Indian Institute of Technology, Indore, Madhya Pradesh, India. ¹¹These authors contributed equally: Nadia A. Erkamp, Mina Farag, Yuanxin Qiu. ✉e-mail: mdleu@wustl.edu; tpjk2@cam.ac.uk; pappu@wustl.edu

shown to arise in simple mixtures³⁰ including ternary systems comprising two different RNA molecules and an arginine-rich peptide³¹.

Increased attention is being paid to interfaces of condensates^{22,32–34}. A recent computational study predicted that in condensates comprising a single type of polymer in a solvent, the polymers that drive condensation, referred to as scaffolds, prefer non-random, orthogonal orientations with respect to the plane of the interface^{33,34}. The solidification of condensates can be nucleated from the interface^{35–38}. Additionally, the electrostatic fields at interfaces³⁹, generated by interphase potentials⁴⁰, can affect condensate fusion⁴¹, catalyze redox reactions⁴², and resist the transport of molecules moving from dilute to dense phase or vice versa⁴³. Notably, RNA molecules can be scaffolds that drive phase separation from the bulk, or they can adsorb onto interfaces of condensates formed by scaffolds. Understanding why specific RNA molecules are scaffolds versus adsorbents is relevant for understanding how RNA-based condensates function in cells⁴⁴. It is also relevant for designing *de novo* condensates based on protein-RNA mixtures.

We investigated the principles underlying spatial organization in condensates formed by ternary mixtures using a model system that comprises a biocompatible polymer, namely polyethylene glycol (PEG)⁴⁵, and pairs of homopolymeric, non-base-pairing RNA molecules such as poly-adenine (poly-rA), which is a poly-purine, and poly-cytosine (poly-rC), which is a poly-pyrimidine⁴⁶. Our investigations were motivated by a general framework anchored in the Gibbs adsorption isotherm⁴⁷, and the physics of adsorption-mediated wetting transitions⁴⁸. We studied adsorption in ternary mixtures, and we investigated the effects of polymer interaction strengths, concentrations, lengths, and stiffness on adsorption. Using Monte Carlo simulations, we quantified the orientation of molecules at the interface that leads to the distinction of condensate components being scaffolds versus adsorbents. We also report results from single-molecule super resolution imaging, which reveals the movement of molecules near the interface. Near the interface, we observed significantly faster motion in the parallel direction than in the perpendicular direction. Finally, we discuss the broader implications of our findings for the design of *de novo* condensates with specific spatial organization and interfacial properties.

Results

Pyrimidine-rich RNA undergoes adsorption and wetting transitions

Heterotypic PEG-RNA interactions provide the driving forces for forming condensates in the model ternary systems^{45,49,50}. Increasing the concentration of PEG alters the chemical potential of PEG and promotes phase separation. Increasing the concentration of NaCl weakens electrostatic repulsions between RNA molecules, and this also promotes phase separation^{40,46}. We first obtained a coarse mapping of the overall phase behaviors as a function of NaCl and PEG concentrations. Poly-rA undergoes phase separation in the presence of sufficient PEG and NaCl (Fig. 1a, b). The concentration of NaCl required to drive phase separation decreases as the concentration of PEG increases, and the slope of the phase boundary becomes zero above 3% w/w of PEG. For these concentrations of PEG, the poly-rA + PEG mixture undergoes phase separation for all NaCl concentrations that are above 0.5M.

While poly-rC also undergoes phase separation, higher amounts of PEG and NaCl are required (Fig. 1c, d). This shows that poly-rA drives phase separation through stronger interactions when compared to poly-rC^{31,46,51}. In these systems where base-pairing is not possible, we reasoned that the double rings of poly-purines make them more hydrophobic and allow for stronger π -stacking than poly-pyrimidines⁵². Stronger interactions in purine-rich systems can also engender dynamically arrested phase separation^{31,46,51}, giving rise to irregular mesoscale structures that are dominated by long-lived intermolecular crosslinks. Here, we observed dynamically arrested

percolated networks for poly-rA and not for poly-rC (Fig. 1b, d)—an observation that is consistent with recent reports⁵³.

Next, we mapped phase boundaries for ternary mixtures of PEG plus a 1:1 ratio of poly-rA and poly-rC (Fig. 1e, g). In the absence of PEG and 0.75 M NaCl, we did not observe phase separation (i, Fig. 1f). Increasing the PEG concentration to 2% w/w, leads to crossing of the phase boundary and formation of a poly-rA-rich phase that coexists with a dilute phase (ii, Fig. 1f). The poly-rC molecules partition into and adsorb onto the interface of the poly-rA-rich phase. The extent of adsorption increased with increasing concentration of PEG (iii, Fig. 1f). When the concentration threshold for forming poly-rC-rich phases was crossed, we observed the formation of three coexisting phases: a dilute phase that coexists with poly-rA- and poly-rC-rich phases, with an interface between the latter two phases (iv, Fig. 1f). Notably, poly-rC still adsorbed to the poly-rA interfaces. The transition from two coexisting phases with adsorption to three coexisting phases is known as a wetting transition⁴⁸.

We observed similar wetting transitions when varying the concentration of NaCl. In 4% PEG and 0.25 M NaCl, the system formed a homogeneous solution (I, Fig. 1g). In the presence of 0.5 M NaCl, poly-rA formed condensates and poly-rC partitioned into and adsorbed onto the interface of the poly-rA-rich phase (II, Fig. 1g). Between 0.75 M and 1.25 M NaCl, we observed what Kaplan et al.⁴⁸ refer to as complete wetting whereby poly-rC formed a well-defined, micron-scale layer at the interface (III–V, Fig. 1g). At 1.5 M NaCl and above, we observed a distinct poly-rC-rich phase that coexists with a poly-rA-rich phase (VI, VII, Fig. 1g). The cascade of transitions we observed for poly-rC can be explained as follows: At low salt concentrations, poly-rC is an adsorbent, forming favorable interactions with PEG molecules at the interface. Increasing the salt concentration beyond the levels that saturate the interface leads to the formation of two coexisting phases defined by favorable poly-rA and PEG interactions (the poly-rA-rich phase) and less favorable poly-rC-PEG interactions, which gives rise to the poly-rC-rich phase. The line scans show the coexistence of poly-rA-rich and poly-rC-rich phases separated by a poly-rC-rich interface (VI VII, Fig. 1g). Note that increasing the salt concentration enhances the heterotypic PEG-poly-rC interactions and homotypic poly-rC interactions.

To assess the transferability of our findings to other systems, we explored the phase behaviors of a range of RNA homopolymers. Specifically, we explored the ability of rA₂₀, rA₈₀, poly-rA, rC₂₀, rC₈₀, poly-rC, rU₂₀, rU₈₀, poly-rU and rG₂₀ to adsorb onto condensates of poly-rA, poly-rC and/or poly-rU with PEG (Figs. S1 and S2). The interaction strengths between the RNA and PEG are influenced by whether the RNA is a poly-pyrimidine or poly-purine. Out of the 35 unique combinations that were explored, we observed a clear trend whereby poly-pyrimidines (rC, rU) adsorb onto dense phases rich in poly-purines. This observation is consistent with the fact that the poly-rA, which is a poly-purine, is a stronger driver of phase separation with PEG (Fig. 1a) when compared poly-rC (Fig. 1c). Taken together, our results suggest that in ternary mixtures, the differences in the relative interaction strengths determine which RNAs are scaffolds and which RNAs are adsorbents that drive phase separation and concentration-dependent wetting transitions.

Adsorbents interact weakly with scaffolds

Next, we compared the relative interaction strengths between PEG and different RNAs by comparing low concentration arms (dashed line) and tie lines of phase diagrams of different ternary mixtures and tie lines (solid lines) (Fig. 2a). A sample with a total composition of Φ_{total} separates into a dilute phase (blue circle with composition Φ_{dilute}) and dense phase (blue square with composition Φ_{dense}). The tie line connects the points Φ_{dilute} , Φ_{total} , and Φ_{dense} . The angle subtended at the intersection of the tie line with the low concentration arm of the phase boundary helps quantify the relative inclusion or exclusion of

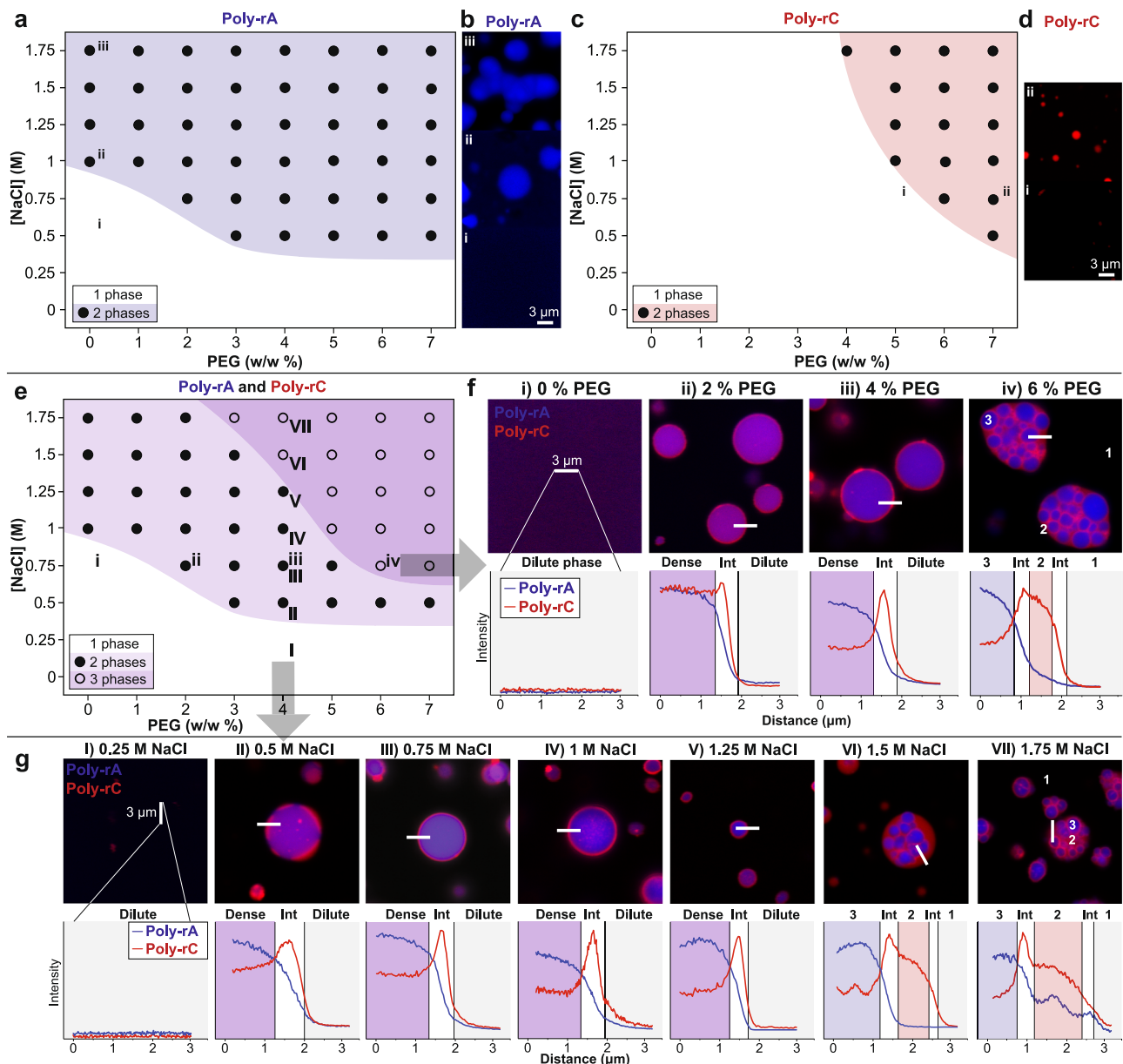


Fig. 1 | Phase separation and adsorption of poly-rA and -rC. **a** Poly-rA (1 g/L) undergoes phase separation in the presence of high concentrations of NaCl and PEG, **b** forming spherical (ii) or irregularly-shaped condensates. **c** poly-rC (1 g/L) phase separation requires higher concentrations of NaCl and PEG **d** to form spherical condensates. **e** The dense phases in a mixture of poly-rA (1 g/L) and poly-rC (1 g/L) show a range of condensate architectures. At low concentrations of PEG (i of **f**) or low concentrations of NaCl (I of **g**) the dense phase is homogenous. Increasing either the concentration of PEG or NaCl, poly-rA forms condensates and some poly-rC is recruited into it (ii of **f**, II of **g**). Notably, poly-rC adsorbs to the

interface. The extent of adsorption increases with increasing concentrations of PEG (iii of **f**) or NaCl (III, IV, V of **g**). At higher concentrations of PEG, for fixed NaCl, or higher concentrations of NaCl for fixed PEG, the adsorbed poly-rC undergoes phase separation leading to a poly-rA-rich phase coexisting with a poly-rC-rich phase. Adsorption of poly-rC around the poly-rA dense phase is still observed (iv of panel **f**, VI and VII of **g**). All scale bars in the confocal images represent 3 μm . Confocal images show representative examples of observations on 50 or more condensates. Source data are provided as a Source Data file—see Data Availability Statement.

molecules in the dilute and dense phases^{49,50}. The slopes of tie lines quantify the relative contributions of homotypic versus heterotypic interactions in the RNA and PEG system. A positive slope points to favorable heterotypic interactions driving the formation of condensates, whereas a negative slope indicates that heterotypic interactions are unfavorable. We mapped phase diagrams using a previously established microfluidics platform^{49,50,54}, creating $\sim 10^4$ samples with varying amounts of RNA and PEG. The approach known as “PhaseScan” scans and sorts of a wide cross section of samples, annotating these as homogeneous (blue) or two-phase systems containing condensates (red). The totality of measurements across the

entire spectrum of PEG and RNA concentrations that were scanned helps in mapping the boundary between the one-phase and two-phase regimes (Fig. 2b). Additionally, we use the concentrations of RNA in the coexisting dilute phase to infer proxies for tie lines (Fig. 2c). This is a way to leverage data from high throughput scanning and estimate a useful proxy for the actual tie line (Fig. S3).

Analysis of the microfluidics data (Fig. S4) helps with delineation of the low concentration arms of phase boundaries for the poly-rA plus PEG (Fig. 2d) and poly-rC plus PEG systems (Fig. 2e). As expected, poly-rA undergoes phase separation at lower PEG concentrations than poly-rC. The slopes of the tie line proxies are positive for both mixtures,

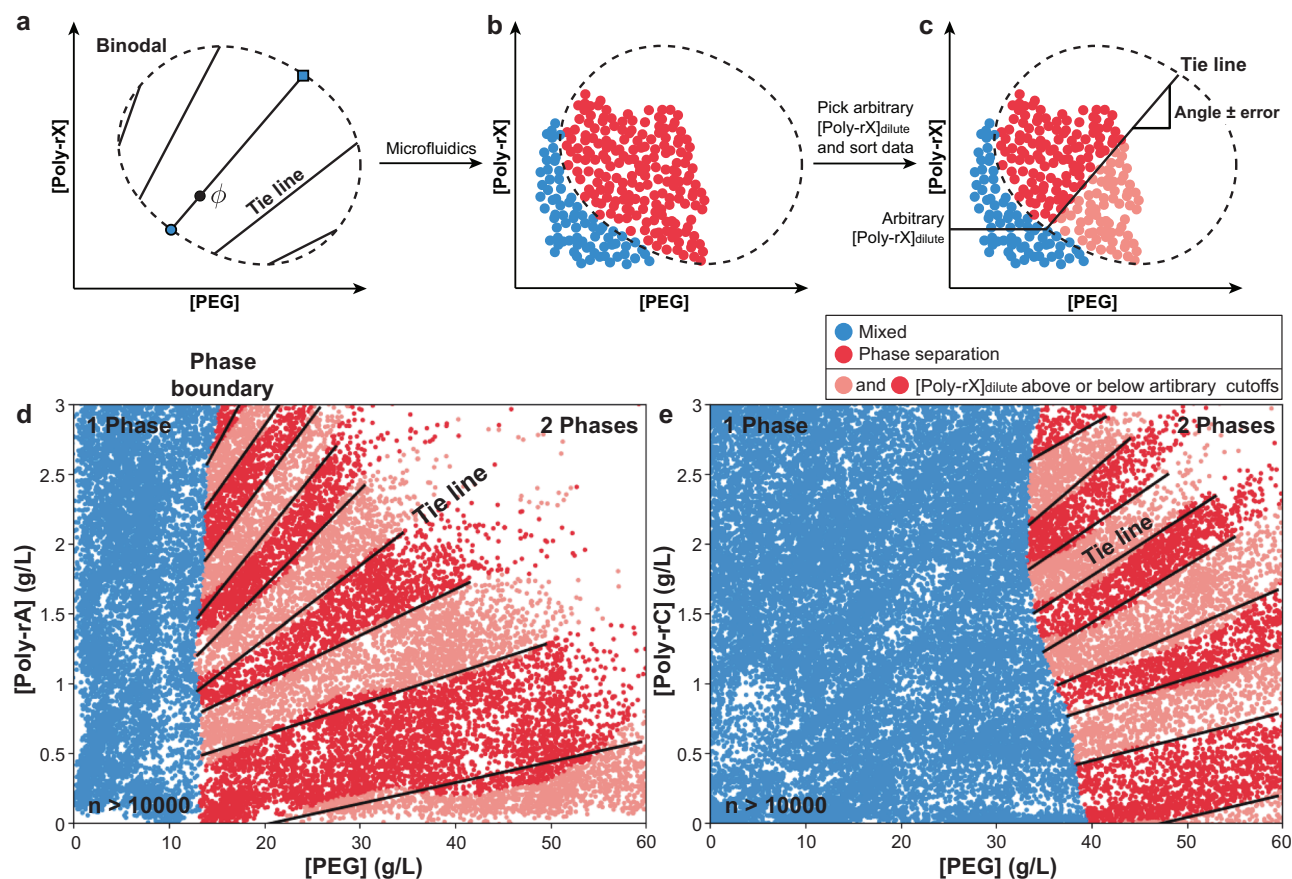


Fig. 2 | Measurements of phase boundaries and tie line proxies using microfluidics. **a** Tie lines show how a sample with total composition ϕ separates into a dilute phase (blue circle) and dense phase (blue square). Tie line angles quantify the repulsion versus attraction of molecules in the two phases (Fig. S3). **b** Using microfluidics (Fig. S4), we can delineate a phase boundary (dashed line) and obtain proxies for tie lines using dilute phase concentrations. Phase diagrams of **d** poly-rA

(1 g/L) and **e** poly-rC (1 g/L) generated using a microfluidic platform. Solid lines show the tie line proxies. Phase separation requires less PEG for poly-rA (**d**), than for poly-rC (**e**). Full lines show a tie line proxy. The tie line proxy of poly-rA with PEG (**c**) is steeper than that of poly-rC with PEG (**d**). This indicates that PEG interacts stronger with poly-rA than with poly-rC. Source data are provided as a Source Data file—see “Data availability” statement.

indicating favorable heterotypic interactions between RNA and PEG and partitioning of both PEG and RNA into the dense phases. Notably, tie line proxies for poly-rA with PEG are larger than for poly-rC with PEG. This implies that the favorable interactions between poly-rA and PEG are stronger than the favorable interactions for poly-rC with PEG^{49,50}.

Taken together with the data in Fig. 1, we arrive at a phenomenological explanation of the adsorption data. Poly-rA and PEG interact favorably, and this drives phase separation with the dense phases being enriched in both species even at moderate PEG concentrations. The favorable interactions between poly-rC and PEG are weaker when compared with poly-rA. This allows poly-rC to partition into the poly-rA + PEG rich phase. Partitioning of poly-rC into poly-rA-rich phases creates a competition between poly-rA and poly-rC. The latter cannot compete effectively for interactions within the dense phase, and as a result, the partitioning is weak, and it adsorbs onto the interface of the poly-rA-rich phase. At the interface, poly-rC can interact with PEG that is not engaged in interactions with poly-rA.

Overall, the relative strengths of the RNA-PEG interactions determine the identities of the adsorbent versus the scaffold. The adsorbent undergoes a cascade of wetting transitions based on the concentration of the adsorbent. To put these observations on a quantitative footing, we turned to computations to explore how adsorption depends on interaction strengths (Fig. 3), polymer

concentration (Fig. S5), polymer length (Figs. 4 and S6) and polymer stiffness (Fig. S7).

Differential interaction strengths are the main drivers of adsorption

We modeled phase behaviors in polymer mixtures using coarse-grained, single bead per monomer representations as implemented in LaSSI⁵⁵, which is a lattice-based simulation engine (Fig. 3). We simulated mixtures of three distinct homopolymers labeled A, B, and C. These bead-string-bead polymers were designed to be phenomenological mimics of poly-rA, PEG, and poly-rC, respectively. Each bead within a polymer is a Kuhn monomer that occupies a single lattice site. Distances between beads are quantified in terms of lattice units (l.u.) on the cubic lattice. For calibration, if the polymer of interest were to follow Gaussian statistics, then the mean end-to-end distance of a single chain would be $n^{1/2}$ where n is the number of Kuhn monomers that make up the chain. Accordingly, for polymers comprising $n = 100$, 250, 300, or 400 beads, the mean end-to-end distance of Gaussian chain equivalents would be 10 l.u., 15.8 l.u., 17.3 l.u., and 20 l.u., respectively.

Polymer B is parameterized to drive condensate formation via heterotypic interactions with polymers A and C. The microscopic pairwise interactions between monomers of the polymers (ϵ_{x-y}) are -2 k_BT for most combinations, -4 k_BT for B-C and we query the effects of varying the interaction strengths for B-A (Fig. 3a, b, see

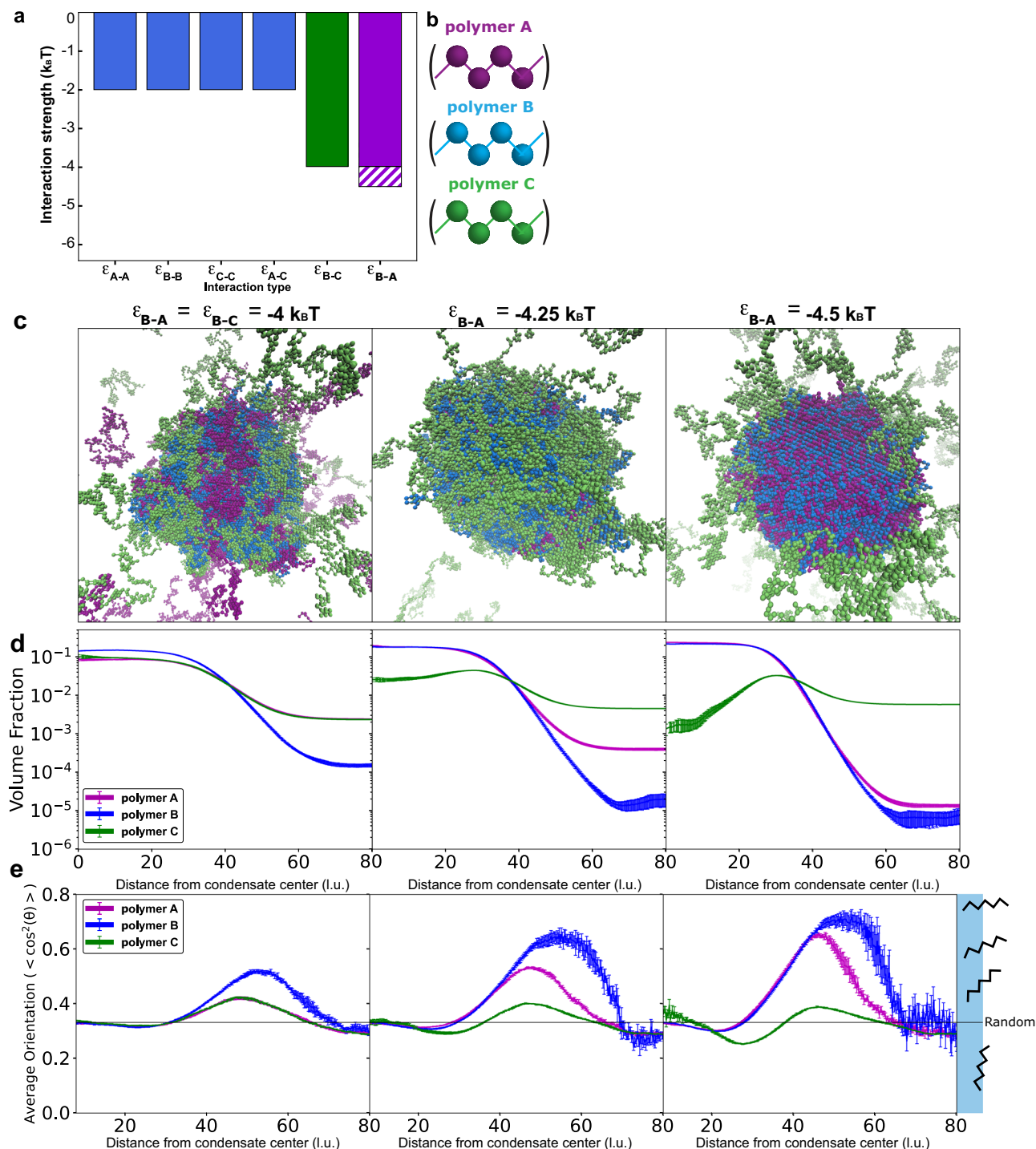


Fig. 3 | Pairwise interaction strengths and relative concentrations determine condensate architectures and interfacial features. **a** The interaction strengths between polymer beads used in the simulations. The interaction between beads of polymers A and B was varied from -4 to -4.5 . **b** Molecules A, B, C represent poly-rA, PEG and poly-rC respectively. **c** Representative snapshots from LaSSI simulations showing distinct condensate architectures obtained by varying the interaction strength between beads of polymers A and B, $|\epsilon_{B-A}| = -4, -4.25, -4.5$. For this same

titration, we show **d** the radial density profiles and **e** the average $\cos^2\theta$ values, which indicate the average orientation of molecules with respect to the center of the condensate (Supplementary Methods). If a given datapoint had an error greater than 0.1, then that datapoint was omitted. In **d** and **e**, error bars indicate the standard errors about the mean across three replicates. Source data are provided—see “Data availability” statement.

Supplementary Material). Here, we used normalized units of $k_B = 1$. By maintaining equivalent polymer concentrations and varying ϵ_{B-A} , we obtained three possible architectures (Fig. 3c, d).

If $|\epsilon_{B-A}| = |\epsilon_{B-C}| = -4 k_B T$, then a uniform dense phase is obtained since A and C are equivalent. For $|\epsilon_{B-A}| = -4.25 k_B T$, the stronger B-A interaction increases the concentration of B and A within the dense

phase and displaces polymer C to the condensate interface and dilute phase. If $|\epsilon_{B-A}| = -4.5 k_B T$, polymer C is mostly excluded from the condensate interior, but its concentration remains highest at the interface. Adsorption is observed for the polymer C characterized by its weaker interaction with the scaffold B. Notably, adsorption is observed in cases where polymer C partitions preferentially into the

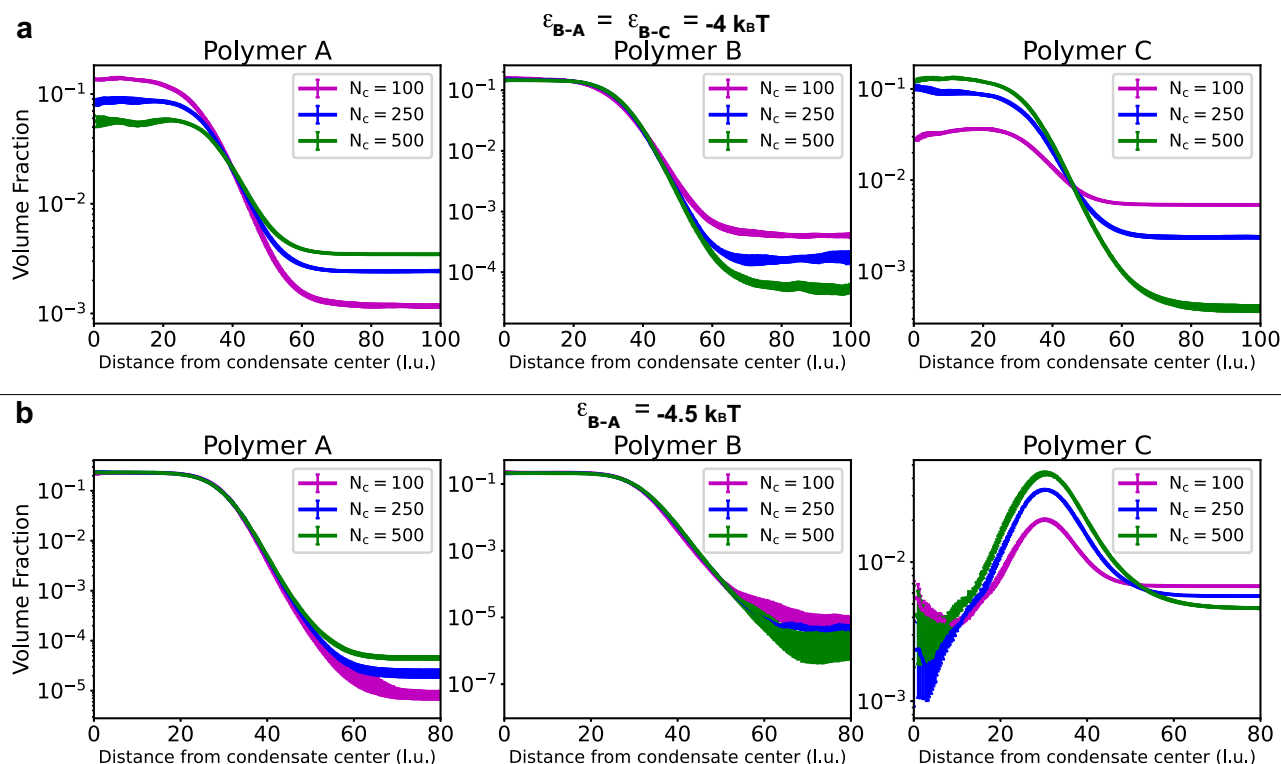


Fig. 4 | Polymer length has a limited effect on condensate architecture in comparison to pairwise interaction strengths. The interaction between beads of polymers A and B was set to **a** $|\epsilon_{B-A}| = -4$, or **b** $|\epsilon_{B-A}| = -4.5$. The volume fractions for the three polymers are shown as a function of the distance from the center of the condensate (similar to Fig. 3d). We observe that molecule length affects partitioning into dilute or dense phase. Notably, varying length does not cause polymer

C to **a** adsorb when it previously did not, or **b** stop adsorbing when it previously did. The interaction strength between the monomers has a much more extensive effect on condensate architecture and interface organization than the length of the polymer. If a given datapoint had an error greater than 0.1, then that datapoint was omitted. Error bars indicate the standard errors about the mean across three replicates. Source data are provided—see “Data availability” statement.

dense phase over the dilute phase (ii) and where it partitions preferentially into the dilute phase over the dense phase (iii).

For $|\epsilon_{B-A}| = -4.5 k_B T$, we investigated the effect of polymer concentration on adsorption. Simulations were performed with 100 molecules of A and B, with 0, 10, 25, 50, 100, and 200 molecules of C (Fig. S5a–f). Molecules of C adsorb preferentially to the interface, with very similar partitioning irrespective of concentration over this range. Increasing the number of A molecules or decreasing the number of B molecules reduces the number of interactions B can have with C thus increasing the dilute phase concentration of C (Fig. S5g, h). Decreasing the number of A molecules and increasing the number of B molecules has the opposite effect, increasing the partitioning of C in the dense phase (Fig. S5i, j). Notably, while partitioning is affected, molecules of C still adsorb, albeit weakly, to the interface, highlighting the importance of monomer interaction strength over polymer concentration.

Next, we consider the effect of polymer length on adsorption (Figs. S6 and S7). For molecules with a length of 250, $|\epsilon_{B-A}| = -4 k_B T$ does not result in adsorption (Fig. 4d). Varying the length of the molecules can change the partitioning of the molecules but it does not cause polymer C to adsorb to the interface (Figs. 4a and S6). Starting in a situation where we observe adsorption for molecules with a length of 250, $|\epsilon_{B-A}| = -4.5 k_B T$, varying the length of the polymers again affects partitioning (Fig. S7). Notably, it does not prevent polymer C from adsorbing (Fig. 4b). We concluded that relative interaction strengths are the most important variable in determining whether polymers adsorb to interfaces.

We also considered the effect of polymer stiffness on adsorption (Fig. S8). We varied molecule stiffness using a bond angle potential of the form: $u(1 - \cos^2\theta)$. Here, θ is the bond angle at the intersection of

three consecutive beads in a chain and u quantifies the amplitude of the stiffness. For flexible polymers, we set $u=0$ whereas for stiff polymers, we set $u=200$. As with flexible polymers, setting $|\epsilon_{B-A}| = -4 k_B T$, does not lead to adsorption even for stiff polymers (Fig. S8a–f). As far as adsorption is concerned, the results for $|\epsilon_{B-A}| = -4.5 k_B T$ are equivalent for stiff versus flexible polymers (Fig. S8a, g, h). We conclude that of the four variables considered, relative monomer interaction strength is the key determinant of condensates architecture with respect to adsorption.

Adsorbents and scaffolds are oriented differently at the interfaces of condensates

Farag et al.³³ introduced an order parameter to quantify the orientation of polymers with respect to the interfaces of condensates. In their simulations, the system had only one type of polymer. We adapted their approach and analyzed the simulations to determine the orientations of polymers A, B and C in our simulations (Fig. 3e). Note that the solvent is pseudo implicit, defined by an absence of direct interactions, but the vacant sites on the lattice do represent solvent molecules. Specifically, we determined the angle θ swept out by the condensate center-of-mass, a given polymer bead i , and another bead on the same polymer that is exactly 100 beads apart from bead i . If θ is close to 0° or 180° , which corresponds to $\cos^2\theta$ values close to 1, then the 100-bead segment is perpendicular to the interface. In contrast, if θ is close to 90° , which corresponds to $\cos^2\theta$ values close to 0, then the 100-bead segment is essentially parallel to the interface. In the case of a polymer that has a random orientation, $\cos^2\theta = 0.33$ (Fig. S5k).

When $|\epsilon_{B-A}| = |\epsilon_{B-C}| = -4 k_B T$, all polymers have random orientations, except at the interface, where there is a bias toward

perpendicular orientations. We also computed the orientational preferences in the case of adsorption realized for $|\epsilon_{B-A}| = -4.25$ or -4.5 k_BT. In the dense and dilute phases, orientations are random. However, at the interface, polymer A and B have an enhanced perpendicular orientation. At the highest concentration of polymer C, ~30 l.u. from the center of the condensate, we observe that polymer C has a more parallel orientation. These results suggest that in a quaternary system with three types of polymers and a pseudo implicit solvent, polymers that behave as scaffolds, namely polymers A and B, minimize the overall interfacial free energy density by adopting more orthogonal orientations at the interface. In contrast, the homopolymer C contributes to minimizing the overall interfacial free energy density by preferring a more parallel orientation. Condensate formation by the scaffold molecules A and B drives a more parallel orientation for molecules of type C because the relative interaction strengths are such that $|\epsilon_{B-A}| > |\epsilon_{B-C}|$.

Taken together with published work, the following rules emerge regarding the orientational preferences of different types of molecules at interfaces of different types of condensates. In a two-component system comprising a single type of polymer in a solvent, enhancing the driving forces for phase separation leads to a diminished preference for more perpendicular orientations of the polymer and an increased preference for more parallel orientations at the interface^{34,56}. These results imply that there are two distinct ways to minimize the interfacial free energy density in the polymer plus solvent systems. One, which is realized via a preference for more perpendicular orientations, helps maximize the number of polymer sections at the interface while minimizing the number density of unsatisfied interactions per chain. The second, which becomes necessary as the driving forces for phase separation become stronger, is a preference for more parallel orientations. This limits the number of chains at the interface while maximizing the interfacial area covered by each chain. In the quaternary systems comprising three types of polymers and a solvent, the scaffold polymers which are stronger drivers of phase separation prefer a more perpendicular orientation when compared to the adsorbent polymers, which prefer more parallel orientations. The adsorbent provides coverage of the interface. This allows for scaffolds to prefer a more perpendicular orientation because it reduces the number density of scaffold segments that need to be exposed at the interface. Thus, the adsorbent thus provides a degree of freedom that is absent in the binary mixture comprising a single type of polymer and a solvent. It is worth emphasizing that scaffolds and adsorbents will align in directions that are both perpendicular and parallel to the interface, with there being a statistical preference of the adsorbents for more parallel orientations.

Observations of anisotropic motions near condensate interfaces

To further investigate interfacial properties of the condensates, we leveraged advances in single-molecule tracking which allowed us to ask if molecules near the interface display anisotropic motions^{57–60}. Specifically, we tracked the movement of single poly-rA molecules (blue) in condensates near interfaces (Fig. 5a). YO-PRO-1 (oxazole yellow) is an RNA binding dye which can diffuse into a poly-rA condensate and intercalate with the RNA. Under continuous excitation, YO-PRO-1 is dark and only emits fluorescence while bound to RNA, due to its fluorogenic nature (yellow squares)^{61,62}. Over time, and depending on the laser power, some of the dyes can be bleached (black square). At low laser power, the poly-rA-rich phase is bright, while the dilute phase is dim (i, Fig. 5b). Increasing the laser power results in significant bleaching and the middle of the poly-rA-rich phase becomes dark (ii, Fig. 5b). At very high laser power, we observe YO-PRO-1 molecules mostly near the interface, which corresponds to a full width at half maximum of ~123 nm. This is due to the combination of constant bleaching and new dye molecules entering the condensate via the interface (iii, Fig. 5b).

The high laser power allowed us to track single YO-PRO-1 molecules using 10 ms camera frames and eliminated signals further away from the interface. We interpret a continuous burst of fluorescence as a single YO-PRO-1 molecule emitting while bound to a single poly-rA molecule before photobleaching or dissociation. We thus obtained trajectories of the poly-rA molecules, which we converted from displacements in the x and y-directions to displacements parallel or perpendicular to the interface for each 10 ms step (Fig. 5c, d). Aligning the origin of each displacement to a common location, we were able to track the movement of molecules (Fig. 5e). To ensure an unambiguous separation between the condensate interior and interface, we chose a segmentation threshold that guards against finite size artifacts, and we split the displacement data into two segments that are within 300 nm of the interface (Fig. 5f) and further away from the interface (Figs. 5g and S9). All inferences regarding the interface come from the data segment within 300 nm of the interface. However, the interface itself is made up of a region that is at the outermost edge of the condensate, constituting a 50 nm band that can be accessed via single fluorogen tracking. We fit the trajectories constituting 10⁴ displacements to a 2D Gaussian obtaining the mean and standard deviation (ellipses) traversed in the parallel and perpendicular directions from the starting location (black dot). We find that closest to the interface, the movements parallel to the interface are significantly faster than movements perpendicular to the interface. This effect disappears as we track movements that progressed into the interior of the dense phase. Figure 5h shows the standard deviation of poly-rA molecules movement of six condensates near three types of interfaces: poly-rA dense phase with dilute phase (pA-dil, orange), poly-rA dense phase with poly-rC adsorbed to the dilute phase (pA-pC-dil, yellow), and poly-rA dense phase with poly-rC dense phase (pA-pC, purple). These data points are off the diagonal, supporting the conclusion that motions of the dyes parallel to the interface are consistently faster than motions of the dye that are perpendicular to the interface. We did not observe anisotropies of motions within the interior of poly-rA-rich phases (interior rA, dark gray) or inside poly-rA-rich phases that are in contact with poly-rC-rich phases (interior rA-rC, light gray).

Our findings regarding the anisotropies of motions at interfaces are in accord with predictions from theory⁶³. For a sphere near a liquid-liquid interface, a higher drag in the perpendicular direction, which translates to lower speeds in this direction when compared to the parallel direction was predicted as being a consequence of the incompressibility of a fluid-fluid interface^{63–65}. Additionally, the interface may limit movement to the dilute phase and thereby reduce perpendicular motion (Fig. S10).

Discussion

Overall, our findings may be summarized as follows: In ternary mixtures comprising pairs of RNA molecules forming condensates via heterotypic interactions with PEG, we find that pyrimidine-rich RNAs adsorb onto and wet the interfaces of condensates. These results allowed us to classify molecules as scaffolds or adsorbents. The classification is bolstered by simulations that reproduce the phenomenology observed in experiments. From the simulations we learned that the identities of adsorbents versus scaffolds are governed by the relative monomer interaction strengths among different molecules. Overall, in a system comprising molecules A, B, and C where A and C interact favorably with B, we obtain the following results: If the A-B interactions are stronger than the B-C interactions, then the C molecules not only partition into the A-B-rich phase, but they also adsorb onto the interface of the A-B-rich phase. Adsorption appears to be the consequence of a balance whereby the C molecules cannot out-compete the stronger A-B interactions, and they can gain access to B molecules at the interface that are not engaged in interactions with A molecules. Increasing the concentration of the C molecules, such that the threshold for phase separation with B molecules is crossed, leads

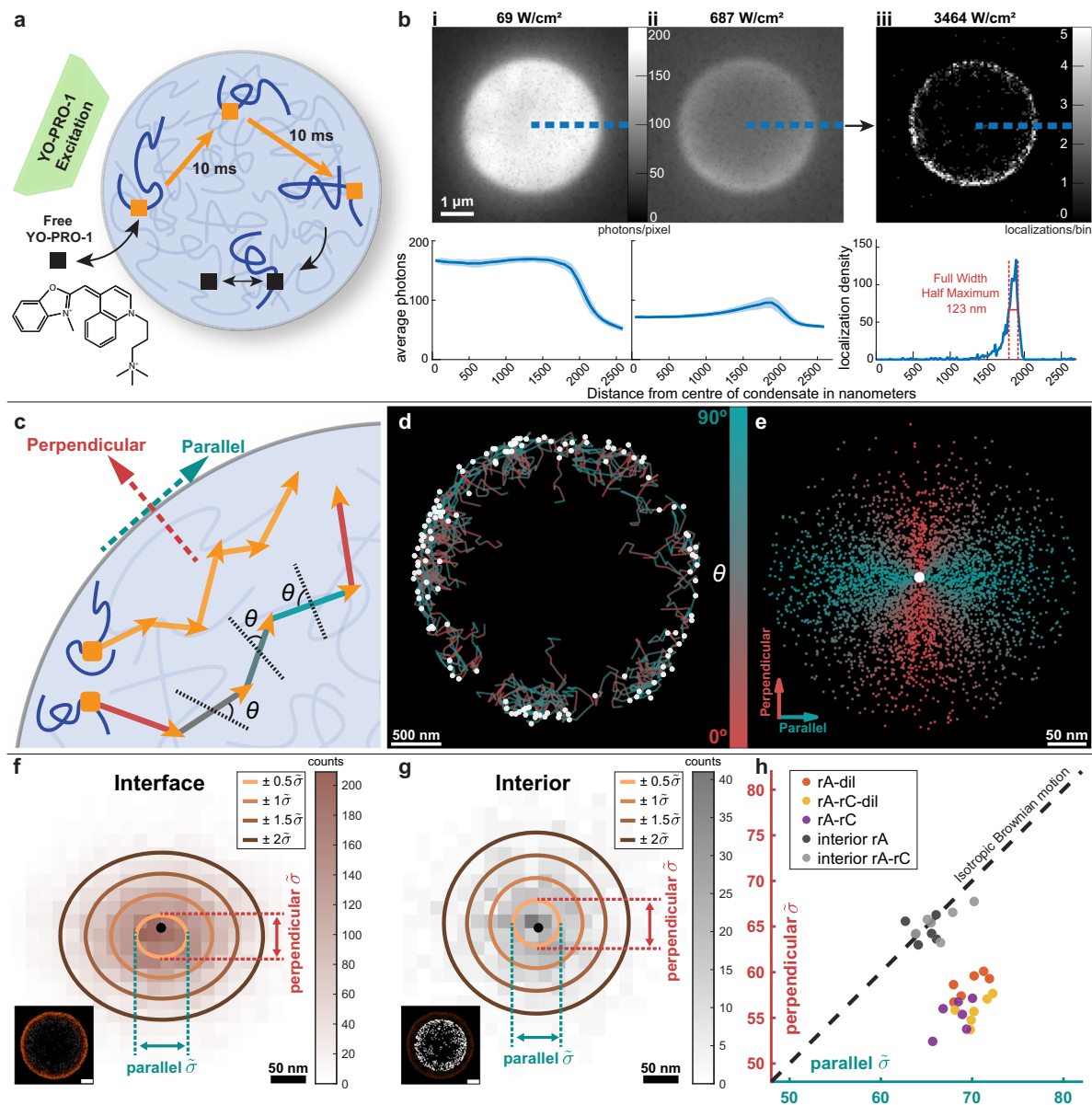


Fig. 5 | Single-molecule tracking near the condensate interface shows anisotropic motion. **a** YO-PRO-1 is a fluorogenic RNA intercalating dye with a strong preference for binding to poly-rA over poly-rC. Initially dark, the dye can move into the condensates and bind to poly-rA to become bright (orange). We track the location of the dye every 10 ms until it is bleached (black). **b** The field of view within the condensate is excited at various laser strengths, bleaching increasingly more bound dye molecules until single molecules can be localized. From diffraction-limited imaging, line profiles (schematized using dashed lines) yield mean (solid) and standard deviation (shaded) of the number of photons/pixel in (i) and (ii). Super-resolution imaging allows quantification of the localization density of YO-PRO-1 near the interface, since the condensate is constantly bleached, and fresh dye molecules move into the condensate through the interface. The histogram in (iii) shows that the full width at half maximum is ~ 123 nm. Six independent experiments were repeated with similar results. **c** The trajectory in the x and y -directions is converted to the displacement parallel (aqua) or perpendicular (red) with respect

to the interface. **d** Trajectories (multiple displacements) of poly-rA molecules in a poly-rA-PEG condensate. **e** Displacements of the trajectories shown in (d). We fit the displacement information with 2D Gaussian distributions for trajectories **f** near interfaces and **g** in the interior of the condensate. **Insets**, scatters of (orange) interface YO-PRO-1 localizations and (gray) interior localizations. **h** The standard deviation in perpendicular and parallel motions for six condensates for trajectories near interfaces: poly-rA dense phase with dilute phase (rA-dil, orange), poly-rA dense phase with poly-rC adsorbed to the dilute phase (rA-rC-dil, yellow), and poly-rA dense phase with poly-rC dense phase (rA-rC, purple). Parallel motions are consistently faster than perpendicular motions. In the interior of poly-rA condensates (interior rA, dark gray) and inside of poly-rA condensates in touch with poly-rC droplets (interior rA-rC, light gray), we observe no anisotropy. Scale bars, **b**, 1 μ m, **d** and **insets of f** and **g**, 500 nm, **e–g**, 50 nm. Source data are provided—see “Data availability” statement.

to a cascade of wetting transitions that eventually lead to A-rich, C-rich, and dilute phases coexisting with one another⁴⁸. While polymer concentration, length and stiffness can affect partitioning into the dense or dilute phases, the computations show that the key determinant of adsorption and condensate architecture is the relative monomer interaction strength.

The computations, which reproduced the phenomenology observed in mesoscale experiments, show that molecules at interfaces have non-random orientational preferences with respect to the planes of interfaces^{22,33}. In the ternary system, where phase separation is designed to be driven by purely heterotypic interactions, the stronger drivers of phase separation have a more perpendicular orientation to

the interface whereas the weaker drivers, which are adsorbents, prefer more parallel orientations. These results contrast with recent discoveries in condensates formed purely via homotypic interactions^{34,56}. There, comparing across different condensates defined by different interaction strengths or valence, the stronger drivers were found to have more parallel orientations compared to weaker drivers^{34,56}. Taken together with work regarding the interplay between homotypic and heterotypic interactions²², our findings suggest that it should be possible to tune condensate architectures and interfacial structures by modulating the relative strengths of scaffold versus adsorbent interactions in multicomponent systems.

Recent studies have shown that the viscoelasticities of condensates can be modeled using graph-theoretic adaptations of the Rouse model that capture the underlying network-like organization of molecules within condensates^{66,67}. The eigenvalues of the graph Laplacians are sufficient for capturing the measured, frequency-dependent viscous and storage moduli^{66,67}. Therefore, it seems reasonable to expect that the interfacial viscoelasticity, which likely originates from interfacial structural anisotropy, also underlies the dynamical anisotropy reported in this work. What is needed are suitable theoretical advancements that enable predictive modeling and reasoning of how adsorbents and scaffolds contribute differently to multiscale structural and dynamical anisotropies in multicomponent condensates. The corpus of simulation results furnished here provides a useful starting point for the development of the relevant theoretical formalism.

The interface is characterized by dynamical anisotropy whereby movement in the parallel direction is faster than in the perpendicular direction. There are three possible explanations for the dynamical anisotropy that we observed using single molecule tracking: The presence of a planar interface, which is a reasonable approximation of the condensate interface at length scales of a probe molecule, will generate higher drag forces in directions that are perpendicular to the interface when compared to the parallel direction⁶³. This comes from the incompressibility of fluid-fluid interfaces. Implicit in this treatment is the contribution of the reduced dimensionality, 2D versus 3D, along the direction that is parallel to the interface^{64,65,68}. Alternatively, differences in viscosity between the dense and dilute phases, which must be balanced at the interface⁶⁹, are also likely to be contributors to the observed dynamical anisotropy. A third scenario pertains to the dynamical anisotropy being determined by the structural anisotropy that combines anisotropy observed on the mesoscale⁷⁰ and the molecular-scale anisotropy that we report in this work.

Our observations, which were derived using generic, biocompatible, and biologically relevant homopolymers, help explain the phenomenology of adsorption that has been reported in cells^{70–72}. Since multiphase condensates create internal interfaces^{27,72}, we propose that the internal interfaces between dense phases might provide additional spatial and temporal control over biochemical interactions. Specifically, interfaces between coexisting dense phases, as well as interfaces between coexisting dilute and dense phases, are likely to provide distinct environments for molecules to accumulate and interact. Adsorption and wetting transitions at interfaces are also relevant for the design of condensates with tunable catalytic functions, given observations from the microdroplet literature which show that reaction efficiencies can be enhanced by orders of magnitude at the interfaces of coexisting phases⁷³. Recent studies have shown that condensates are defined by interphase electric potentials^{15,40}, and this can help set up interfacial electric fields³⁹. In spatially organized condensates, there can be internal and external interfaces that can be engineered to minimize off-target reactions in biochemical reactions involving multi-enzyme pathways⁷³.

Overall, our work shows how rules can be extracted for designing condensates with bespoke interfacial structure and dynamics. Our

results highlight key physical principles that govern the formation of spatially heterogeneous condensates. Additional considerations of site- or chemistry-specific associative interactions are likely to provide further tunability to the spatial organization of macromolecules within and around condensates.

Methods

Materials

Poly-rA (MW 700–3500 kDa, 10108626001), PEG (average MW-20,000), Poly-rC (average MW 118 kDa, P4903), HEPES, NaCl, KCl, ethanol and mPEG(5k)silane were obtained from Sigma Aldrich. Alexa Fluor™ 647 Carboxylic Acid, Alexa Fluor™ 488 Carboxylic Acid and RNAase free water were obtained from Thermo Fisher. PEG(20k)-AF647 was purchased from Nanocs. Sylgard 184 Elastomer base and curing agent were purchased from Dow Corning Corporation. 18 × 18 mm glass slides were purchased from Academy. 24 × 60 mm No.1.5 glass slides were purchased from DWK Life Sciences. (T)₂₀-AF488, (C)₂₀-AF546 and other oligos were purchased from GenScript.

Fabrication of imaging wells for confocal microscopy

The details of the preparation of imaging wells for confocal microscopy are essentially identical to those of Erkamp et al.⁷⁴. As described in that work, we used PDMS slabs of 3 mm in height. These were fabricated by mixing Sylgard 184 Elastomer base and curing agent at a 10:1 ratio and heating at 65 °C for 1.5 h. All additional details are as described in Erkamp et al.⁷⁴. The wells and 18 × 18 mm glass slides used to seal the top of wells were treated with PEG-silane, using a method based on recommended protocols⁷⁵ and previous reports³⁰. The treatment solution was prepared by mixing 10 mg of PEG(5000)silane with 20 µL of glacial acetic acid and 1 mL of ethanol. Wells and glass slides were treated by placing them in solution for 1 h at 65 °C and afterwards washing them thoroughly with water. Treated devices were not used after more than 3 weeks from the time of the initial treatment. These methods were essentially identical to the protocols established in previous work⁷⁴.

Condensate preparation

All condensates were prepared and imaged at room temperature (~20 °C). Condensates of poly-rA and or poly-rC with PEG were prepared by mixing stock solutions in an Eppendorf tube in the following order: PEG, buffer, RNA, salt. All solutions were prepared in RNAase free water. The poly-rA and poly-rC concentrations were determined with a nanodrop machine by measuring the absorbance at 260 nm. Poly-rA and poly-rC were fluorescently labelled by incubation of 0.5 mol% of (T)₂₀-AF488 or (C)₂₀-AF546 for 3 min at 80 °C. The sample was placed in an imaging well and sealed airtight.

Confocal imaging

A Leica Stellaris 5 confocal microscope (confocal fluorescence imaging) (white light laser) microscope equipped with a 63× oil immersion Leica 1.4 NA was used for imaging. Further analysis of pictures was performed using Fiji⁷⁶.

Microfluidic device design and fabrication

Standard lithography processes were used to fabricate the microfluidic devices^{54,77}. The AutoCAD (AutoDesk) software was used to design the devices, which were printed on a photomask (Micro Lithography). A 45 µm layer of SU8-3050 photoresist (Microchem) was spun on a silicon wafer and heated at 95 °C for 15 min. The photomask was placed on top, and the pattern was placed onto the wafer using exposure to UV light and heating at 95 °C for 15 min. Propylene glycol methyl ether acetate (PGMEA) was used to remove excess unreacted SU8-3050. The wafer was dried and a profilometer was used to confirm the height of the device. PDMS at 1:10 curing agent:base ratio was placed on top of the mould and heated at 65 °C for 1.5 h. The PDMS was cleaned, holes

were punched into inlets and outlets, the PDMS substrate was then bonded to glass slides using a plasma oven (30 s, 40% power, Femto, Diener Electronics). The interior of the device was treated with 1% trichloro(1H,1H,2H,2H-perfluorooctyl)silane (Sigma) in HFE-7500 (Fluorochem), before being dried and heated at 95 °C for 1 min.

Mapping phase diagrams and constructing tie-lines

Aqueous droplets in oil of an average volume of 100 pL were created at ~100 droplets per second using a microfluidics setup as shown schematically in Fig. S4. Specifically, a solution of fluorescently labelled 10^4 ng/ μ L poly-rA or poly-rC was mixed with a solution of fluorescently labelled 20% w/w PEG and a solution with buffer at varying rates while a constant amount of KCl solution was added, all of which were being encapsulated in fluorinated oil (HFE-7500 Fluorochem with 1% v/v fluorosurfactant), flowing at constant speed. To flow the solutions into the microfluidic device, syringes (Hamilton 1710) and syringe pumps (neMESYS modules, Cetoni) were used. Syringes were connected to the microfluidic device using tubing (PTFE, 0.012"ID \times 0.030"OD, Cole-Parmer). The 100 pL droplets were created by a total aqueous flow rate of 60 μ L/h and the oil flow rate of 150 μ L/h. After a 5-min incubation period, the aqueous droplets in oil were imaged simultaneously at the wavelength corresponding to poly-rX (488 or 546 nm) and PEG (647 nm). These images were analyzed using a Python program⁵⁴ to determine the concentrations of these compounds and the presence or absence of condensates. Additionally, the dilute phase concentration of poly-rX was determined by calibrating the intensity of 488 or 546 in an area absent of condensates to concentration poly-rX concentration. Each droplet gives information for one datapoint in Fig. 2d or 2e. The boundaries were determined using fitting that is based on support vector machine-based methods. The tie lines were fitted between the datapoints classified as being "condensates" by grouping them based on their poly-rX dilute phase concentration.

Coarse-grained simulations

Simulations were performed using LaSSI, a lattice-based Monte Carlo engine, which allowed us to simulate large condensates without sacrificing efficiency^{22,33,55}. Monte Carlo moves are accepted or rejected based on the Metropolis-Hastings criterion so that the probability of accepting a move is equal to $\min(1, \exp(-\beta\Delta E))$, where $\beta = 1/kT$. Here, kT is the simulation temperature (set to 55 in units of $k = 1$) and ΔE is the change in total system energy associated with the attempted move. Total system energies were calculated using a nearest neighbor model and the following interaction energies: $\epsilon_{A-A} = \epsilon_{B-B} = \epsilon_{C-C} = \epsilon_{A-C} = -2$; $\epsilon_{B-C} = -4$; ϵ_{B-A} was -4 , -4.25 , or -4.5 .

Unless stated otherwise, each simulation involves 10^2 distinct polymers of each type. The lattice spacing is one unit $L = 1$ and the simulation volume is a cubic lattice comprising $150 \times 150 \times 150 = 3.375 \times 10^6$ lattice sites. Each bead of the polymer occupies a single lattice site. In the simplest scenario, each type A, type B, and type C chain is 250 beads long. Therefore, of the 4×10^6 sites available to the polymers, only 7.5×10^4 sites will be occupied at any given instant. Vacant sites represent the solvent. In our analysis of simulation results, all distances between beads within a polymer or between polymers are reported in terms of lattice units and denoted as l.u. For calibration, if a chain has n beads and the chain obeys Gaussian statistics, then its mean end-to-end distance will be $n^{1/2}$. Accordingly, for a chain comprising 250 beads, the mean end-to-end distance of a Gaussian chain will be 15.8 l.u.

The simulations were performed for 5×10^{10} Monte Carlo moves and were allowed to equilibrate such that the chains formed a single condensate with a coexisting dilute phase before any analysis was performed. This simulation length has been shown to be appropriate for systems of the size chosen in our work^{5,22,33,34}. Analyses were only performed using data from the second half of each simulation. Three independent simulations were performed at each condition, and the

results shown are aggregates over all replicates. Radial densities of each polymer type were normalized using the exact number of lattice sites in each radial shell. The condensate center-of-mass was taken to be the center-of-mass of the single largest network of interacting chains. The chain orientation analysis in Fig. 3 was introduced previously^{33,34}. Here, we perform the analysis as follows: (1) for a given chain in the system, find all pairs of beads (i, j) that are exactly 100 beads apart along the chain. (2) For each pair, draw a line segment from the condensate center-of-mass to bead i . (3) Draw a line segment from bead i to bead j . (4) Determine the angle, q , swept out by the two different line segments. (5) Calculate $\cos^2\theta$ and bin this value based on the distance between bead i and the condensate center-of-mass. (6) Repeat steps 1–5 for all chains in the system. (7) For each bin (as described in step 5), we report the average of the calculated $\cos^2\theta$ values. If a given datapoint had an error greater than 0.1, then that datapoint was omitted.

Widefield single-molecule imaging

Widefield images (Fig. 5b) with various excitation laser strengths and single-molecule image stacks (Fig. S9) were acquired with a home-built epifluorescence widefield microscope. Mixtures of 10 μ L condensate systems with YO-PRO-1 solution (wide-field imaging: 0.5 μ L, 1 μ M; single-molecule imaging on poly-rA: 2 μ L, 125 nM; single-molecule imaging on poly-rA-rC: 1 μ L, 500 nM) were loaded in silicone wells (Grace Bio-Labs 665206) on cover glass and sealed to prevent evaporation for imaging. A 488 nm excitation laser (Coherent OBIS LX) was collimated above an oil-immersion objective (OLYMPUS UPLSA-PO100XOPSF, NA 1.4) to illuminate the sample, and the emitted fluorescence is collected with the same objective. A dichroic mirror (Semrock FF01-523/610-25) and an emission filter (Semrock FF01-593/46) were employed for maximizing the fluorescence signal-to-background ratio. Similar to Wu et al.³⁴ a polarizing beamsplitter split the fluorescence into two orthogonally polarized channels, and each channel was focused onto non-overlapping regions of a Photometrics Prime BSI sCMOS camera controlled via Micro-Manager (v.2.0.3). For single-molecule imaging, high-intensity illumination (~ 4850 W cm⁻² peak) was used. Single-molecule images of YO-PRO-1 were acquired with a 10-ms exposure time for 20,000 frames for an average of ~400 photons per localization within each frame. Single-molecule imaging experiments were repeated on 6 individual condensates of each condensate system.

Single-molecule image analysis, localizations and tracking

Localization and tracking of individual molecules was performed following the work of Wu et al.³⁴ where we applied the same Robust Statistical Estimation algorithm (RoSE-O)⁷⁸ and registered the two polarized imaging channels as described previously. A Poisson maximum likelihood estimator was used to fit the standard point spread function to the single-molecule images and measure the lateral position, orientation, and brightness of each molecule. Our localization algorithm has ~16 nm localization precision. This theoretical precision is evaluated for the average fluorescence signal (400 photons) and background (8 photons/pixel) from measured events. We did not observe any YO-PRO-1 with strong orientation preferences.

All position estimates were subsequently classified and grouped into single-molecule trajectories. Molecular movements were tracked by connecting single-molecule positions between consecutive frames. Estimates from two consecutive frames were classified as the same molecule if: 1) they are the closest pair of estimates between the frames, and 2) their distance d is within the confinement radius $d < 200$ nm. All distances are computed in Euclidean form.

Directional displacements between each 10 ms frame and the average position of each molecule's trajectory (termed a molecule's position) were computed. The condensate interface curvature is determined by fitting a circle to the positions of a subset of molecules

(>90th percentile of those furthest from the condensate center). The deformed curvatures on poly-rA-rC condensates from different interface types (pA-pC or pA-pC-dil) were manually separated and then fitted with the corresponding circles. Directional displacements were converted into parallel and perpendicular relative to the fitted interface curvature and aligned to a common position on the interface. Independent 2D Gaussian fits were performed on directional displacement histograms in parallel-perpendicular coordinates.

Statistics and reproducibility

Figures 1, S1, S2, S4 and S9 show representative images. Other condensates or places in the sample (>50) were observed to show similar architectures/behavior. Figure 2c, d contain information from over 10⁴ samples (~100 pL each). The fitted phase boundaries match with phase boundaries observed for larger samples (10–100 μ L, Fig. 1). Figures 3, 4, S5, S6, S7 and S8 show the mean across three replicates and error bars indicating the standard errors. Figure 5b, d, e shows data collected by imaging a poly-rA condensate over 2.5 s. Figure 5h shows the results from 6 condensates for 3 different interfaces and 2 interiors, analyzed similar to shown in 5d–g. Supplementary Table 1 shows how many displacements were analyzed for each of these events (Fig. S9). Single molecules blinking at the interface was observed in >50 condensates in all samples.

Reporting summary

Further information on research design is available in the Nature Portfolio Reporting Summary linked to this article.

Data availability

All the data used to generate all the figure panels are available via the ZENODO repository [<https://doi.org/10.5281/ZENODO.15042167>]. Due to the size of the dataset, we have not included the raw data from the Monte Carlo simulations or the single-molecule imaging experiments. These data are available on request from the corresponding authors: mdlew@wustl.edu; tpjk2@cam.ac.uk; pappu@wustl.edu. Unless otherwise stated, all data supporting the results of this study can be found in the article, supplementary, and source data files. Source data are provided with this paper.

Code availability

All code used to analyze the simulations is available via [<https://github.com/Pappulab/Data-and-analysis-for-RNA-Interfaces>]. The original version of this repository is available at [<https://doi.org/10.5281/zenodo.15042167>]. Simulations were performed using LaSSI, which is available via [<https://github.com/Pappulab/LASSI>]⁵⁵. Single-molecule data were analyzed using RoSE-O, and all the code is available via [<https://github.com/Lew-Lab/RoSE-O>].

References

- Banani, S. F., Lee, H. O., Hyman, A. A. & Rosen, M. K. Biomolecular condensates: organizers of cellular biochemistry. *Nat. Rev. Mol. Cell Biol.* **18**, 285–298 (2017).
- Shin, Y. & Brangwynne, C. P. Liquid phase condensation in cell physiology and disease. *Science* **357**, eaaf4382 (2017).
- Pappu, R. V., Cohen, S. R., Dar, F., Farag, M. & Kar, M. Phase transitions of associative biomacromolecules. *Chem. Rev.* **123**, 8945–8987 (2023).
- Lin, A. Z. et al. Dynamical control enables the formation of demixed biomolecular condensates. *Nat. Commun.* **14**, 7678 (2023).
- Feric, M. et al. Mesoscale structure–function relationships in mitochondrial transcriptional condensates. *Proc. Natl. Acad. Sci. USA* **119**, e2207303119 (2022).
- Simon, J. R., Carroll, N. J., Rubinstein, M., Chilkoti, A. & López, G. P. Programming molecular self-assembly of intrinsically disordered proteins containing sequences of low complexity. *Nat. Chem.* **9**, 509–515 (2017).
- Roberts, S. et al. Injectable tissue integrating networks from recombinant polypeptides with tunable order. *Nat. Mater.* **17**, 1154–1163 (2018).
- Simon, J. R., Eghtesadi, S. A., Dzuricky, M., You, L. & Chilkoti, A. Engineered ribonucleoprotein granules inhibit translation in protocoils. *Mol. Cell* **75**, 66–75.e65 (2019).
- Zeng, X., Holehouse, A. S., Chilkoti, A., Mittag, T. & Pappu, R. V. Connecting coil-to-globule transitions to full phase diagrams for intrinsically disordered proteins. *Biophys. J.* **119**, 402–418 (2020).
- Dai, Y. et al. Programmable synthetic biomolecular condensates for cellular control. *Nat. Chem. Biol.* **19**, 518–528 (2023).
- Rana, U. et al. Asymmetric oligomerization state and sequence patterning can tune multiphase condensate miscibility. *Nat. Chem.* **16**, 1073–1082 (2024).
- Lee, D. S. W., Wingreen, N. S. & Brangwynne, C. P. Chromatin mechanics dictates subdiffusion and coarsening dynamics of embedded condensates. *Nat. Phys.* **17**, 531–538 (2021).
- Fritsch, A. W. et al. Local thermodynamics govern formation and dissolution of *Caenorhabditis elegans* P granule condensates. *Proc. Natl. Acad. Sci. USA* **118**, e2102772118 (2021).
- Su, X. et al. Phase separation of signaling molecules promotes T cell receptor signal transduction. *Science* **352**, 595–599 (2016).
- King, M. R. et al. Macromolecular condensation organizes nucleolar sub-phases to set up a pH gradient. *Cell* **187**, 1889–1906.e1824 (2024).
- Yang, P. et al. G3BP1 is a tunable switch that triggers phase separation to assemble stress granules. *Cell* **181**, 325–345.e328 (2020).
- Riback, J. A. et al. Composition-dependent thermodynamics of intracellular phase separation. *Nature* **581**, 209–214 (2020).
- Sanders, D. W. et al. Competing protein–RNA interaction networks control multiphase intracellular organization. *Cell* **181**, 306–324.e328 (2020).
- Guillen-Boixet, J. et al. RNA-induced conformational switching and clustering of G3BP drive stress granule assembly by condensation. *Cell* **181**, 346–361.e317 (2020).
- Martin, E. W. et al. Valence and patterning of aromatic residues determine the phase behavior of prion-like domains. *Science* **367**, 694–699 (2020).
- Bremer, A. et al. Deciphering how naturally occurring sequence features impact the phase behaviours of disordered prion-like domains. *Nat. Chem.* **14**, 196–207 (2022).
- Farag, M., Borchers, W. M., Bremer, A., Mittag, T. & Pappu, R. V. Phase separation of protein mixtures is driven by the interplay of homotypic and heterotypic interactions. *Nat. Commun.* **14**, 5527 (2023).
- Welles, R. M. et al. Determinants that enable disordered protein assembly into discrete condensed phases. *Nat. Chem.* **16**, 1062–1072 (2024).
- Xing, W., Muhlrad, D., Parker, R. & Rosen, M. K. A quantitative inventory of yeast P body proteins reveals principles of composition and specificity. *eLife* **9**, e56525 (2020).
- Decker, C. J. & Parker, R. P-bodies and stress granules: possible roles in the control of translation and mRNA degradation. *Cold Spring Harb. Perspect. Biol.* **4**, a012286 (2012).
- Tauber, D. et al. Modulation of RNA condensation by the DEAD-box protein eIF4A. *Cell* **180**, 411–426.e416 (2020).
- Feric, M. et al. Coexisting liquid phases underlie nucleolar sub-compartments. *Cell* **165**, 1686–1697 (2016).
- Lafontaine, D. L. J., Riback, J. A., Bascetin, R. & Brangwynne, C. P. The nucleolus as a multiphase liquid condensate. *Nat. Rev. Mol. Cell Biol.* **22**, 165–182 (2021).

29. Fei, J. et al. Quantitative analysis of multilayer organization of proteins and RNA in nuclear speckles at super resolution. *J. Cell Sci.* **130**, 4180–4192 (2017).
30. Lu, T. & Spruijt, E. Multiphase complex coacervate droplets. *J. Am. Chem. Soc.* **142**, 2905–2914 (2020).
31. Boeynaems, S. et al. Spontaneous driving forces give rise to protein-RNA condensates with coexisting phases and complex material properties. *Proc. Natl. Acad. Sci. USA* **116**, 7889–7898 (2019).
32. Chauhan, G., Farag, M., Cohen, S. R. & Pappu, R. V. Reply to: the conformations of protein chains at the interface of biomolecular condensates. *Nat. Commun.* **15**, 9974 (2024).
33. Farag, M. et al. Condensates formed by prion-like low-complexity domains have small-world network structures and interfaces defined by expanded conformations. *Nat. Commun.* **13**, 7722 (2022).
34. Wu, T. et al. Single-fluorogen imaging reveals distinct environmental and structural features of biomolecular condensates. *Nat. Phys.* (2025).
35. Shen, Y. et al. Biomolecular condensates undergo a generic shear-mediated liquid-to-solid transition. *Nat. Nanotechnol.* **15**, 841–847 (2020).
36. Linsenmeier, M. et al. The interface of condensates of the hnRNP1 low-complexity domain promotes formation of amyloid fibrils. *Nat. Chem.* **15**, 1340–1349 (2023).
37. Choi, C.-H., Lee, D. S. W., Sanders, D. W. & Brangwynne, C. P. Condensate interfaces can accelerate protein aggregation. *Biophys. J.* **123**, 1404–1413 (2024).
38. Emmanouilidis, L. et al. A solid beta-sheet structure is formed at the surface of FUS droplets during aging. *Nat. Chem. Biol.* **20**, 1044–1052 (2024).
39. Hoffmann, C. et al. Electric potential at the interface of membraneless organelles gauged by graphene. *Nano Lett.* **23**, 10796–10801 (2023).
40. Posey, A. E. et al. Biomolecular condensates are characterized by interphase electric potentials. *J. Am. Chem. Soc.* **146**, 28268–28281 (2024).
41. Welsh, T. J. et al. Surface electrostatics govern the emulsion stability of biomolecular condensates. *Nano Lett.* **22**, 612–621 (2022).
42. Dai, Y. et al. Interface of biomolecular condensates modulates redox reactions. *Chem* **9**, 1594–1609 (2023).
43. Zhang, Y. et al. The exchange dynamics of biomolecular condensates. *eLife* **12**, RP91680 (2024).
44. Roden, C. & Gladfelter, A. S. RNA contributions to the form and function of biomolecular condensates. *Nat. Rev. Mol. Cell Biol.* **22**, 183–195 (2021).
45. André, A. A. M., Yewdall, N. A. & Spruijt, E. Crowding-induced phase separation and gelling by co-condensation of PEG in NPM1-rRNA condensates. *Biophys. J.* **122**, 397–407 (2022).
46. Wadsworth, G. M. et al. RNAs undergo phase transitions with lower critical solution temperatures. *Nat. Chem.* **15**, 1693–1704 (2023).
47. Scatchard, G. The Gibbs Adsorption Isotherm. *J. Phys. Chem.* **66**, 618–620 (1962).
48. Kaplan, W. D., Chatain, D., Wynblatt, P. & Carter, W. C. A review of wetting versus adsorption, complexions, and related phenomena: the rosetta stone of wetting. *J. Mater. Sci.* **48**, 5681–5717 (2013).
49. Qian, D. et al. Tie-line analysis reveals interactions driving heteromolecular condensate formation. *Phys. Rev. X* **12**, 041038 (2022).
50. Qian, D. et al. Dominance analysis to assess solute contributions to multicomponent phase equilibria. *Proc. Natl. Acad. Sci. USA* **121**, e2407453121 (2024).
51. Alshareedah, I. et al. Interplay between short-range attraction and long-range repulsion controls reentrant liquid condensation of ribonucleoprotein–RNA complexes. *J. Am. Chem. Soc.* **141**, 14593–14602 (2019).
52. Sigel, A., Operschall, B. P. & Sigel, H. Comparison of the π -stacking properties of purine versus pyrimidine residues. Some generalizations regarding selectivity. *JBIC* **19**, 691–703 (2014).
53. Mahendran, T. S., Wadsworth, G. M., Singh, A., Gupta, R. & Banerjee, P. R. Biomolecular condensates can enhance homotypic RNA clustering. *Nature Chemistry* **In press**, 2024.2006.2011.598371 (2025).
54. Arter, W. E. et al. Biomolecular condensate phase diagrams with a combinatorial microdroplet platform. *Nat. Commun.* **13**, 7845 (2022).
55. Choi, J.-M., Dar, F. & Pappu, R. V. LASSI: a lattice model for simulating phase transitions of multivalent proteins. *PLOS Comput. Biol.* **15**, e1007028 (2019).
56. von Bülow, S., Tesei, G. & Lindorff-Larsen, K. Prediction of phase separation propensities of disordered proteins from sequence. *bioRxiv* **2024**, 597109 (2024).
57. Ding, T., Wu, T., Mazidi, H., Zhang, O. & Lew, M. D. Single-molecule orientation localization microscopy for resolving structural heterogeneities between amyloid fibrils. *Optica* **7**, 602–607 (2020).
58. Lu, J., Mazidi, H., Ding, T., Zhang, O. & Lew, M. D. Single-molecule 3D orientation imaging reveals nanoscale compositional heterogeneity in lipid membranes. *Angew. Chem. Int. Ed.* **59**, 17572–17579 (2020).
59. Zhang, O. & Lew, M. D. Single-molecule orientation localization microscopy II: a performance comparison. *J. Opt. Soc. Am. A* **38**, 288–297 (2021).
60. Ding, T. & Lew, M. D. Single-molecule localization microscopy of 3D orientation and anisotropic wobble using a polarized vortex point spread function. *J. Phys. Chem. B* **125**, 12718–12729 (2021).
61. Rye, H. S. et al. Stable fluorescent complexes of double-stranded DNA with bis-intercalating asymmetric cyanine dyes: properties and applications. *Nucleic Acids Res.* **20**, 2803–2812 (1992).
62. Carlsson, C., Larsson, A., Jonsson, M., Albinsson, B. & Norden, B. Optical and photophysical properties of the oxazole yellow DNA probes YO and YOYO. *J. Phys. Chem.* **98**, 10313–10321 (1994).
63. Lee, S. H., Chadwick, R. S. & Leal, L. G. Motion of a sphere in the presence of a plane interface. Part 1. An approximate solution by generalization of the method of Lorentz. *J. Fluid Mech.* **93**, 705–726 (1979).
64. Villa, S., Boniello, G., Stocco, A. & Nobili, M. Motion of micro- and nano- particles interacting with a fluid interface. *Adv. Colloid Interface Sci.* **284**, 102262 (2020).
65. Benavides-Parra J. C., Jacinto-Méndez D., Brotons G., Carbajal-Tinoco M. D. Brownian motion near a liquid-gas interface. *J. Chem. Phys.* **145**, 114902 (2016).
66. Cohen, S. R., Banerjee, P. R. & Pappu, R. V. Direct computations of viscoelastic moduli of biomolecular condensates. *J. Chem. Phys.* **161**, 095103 (2024).
67. Alshareedah, I. et al. Sequence-specific interactions determine viscoelasticity and ageing dynamics of protein condensates. *Nat. Phys.* **20**, 1482–1491 (2024).
68. Adam, G. & Delbrück, M. Reduction of dimensionality in biological diffusion processes. *Struct. Chem. Mol. Biol.* **198**, 198–215 (1968).
69. Dahiya, P., Caggioni, M. & Spicer, P. T. Arrested coalescence of viscoelastic droplets: polydisperse doublets. *Philos. Trans. R. Soc. A Math. Phys. Eng. Sci.* **374**, 20150132 (2016).
70. Law, J. O. et al. A bending rigidity parameter for stress granule condensates. *Sci. Adv.* **9**, eadg0432 (2023).
71. Kusumaatmaja, H. et al. Wetting of phase-separated droplets on plant vacuole membranes leads to a competition between tonoplast budding and nanotube formation. *Proc. Natl. Acad. Sci. USA* **118**, e2024109118 (2021).
72. Wang, Y. et al. Biomolecular condensates mediate bending and scission of endosome membranes. *Nature* **634**, 1204–1210 (2024).

73. Stroberg, W. & Schnell, S. Do cellular condensates accelerate biochemical reactions? lessons from microdroplet chemistry. *Bio-phys. J.* **115**, 3–8 (2018).
74. Erkamp, N. A. et al. Spatially non-uniform condensates emerge from dynamically arrested phase separation. *Nat. Commun.* **14**, 684 (2023).
75. Alberti, S., Gladfelter, A. & Mittag, T. Considerations and challenges in studying liquid-liquid phase separation and biomolecular condensates. *Cell* **176**, 419–434 (2019).
76. Schindelin, J. et al. Fiji: an open-source platform for biological-image analysis. *Nat. Methods* **9**, 676–682 (2012).
77. Mazutis, L. et al. Single-cell analysis and sorting using droplet-based microfluidics. *Nat. Protoc.* **8**, 870–891 (2013).
78. Mazidi, H., King, E. S., Zhang, O., Nehorai, A. & Lew, M. D. Dense super-resolution imaging of molecular orientation via joint sparse basis deconvolution and spatial pooling. In *Proc. 2019 IEEE 16th International Symposium on Biomedical Imaging (ISBI 2019)* (IEEE, 2019).

Acknowledgements

This work was funded by an EMBO fellowship (ALTF 772-2024, N.A.E.), the Royall Scholarship (N.A.E.), the Center for Biomolecular Condensates at Washington University in St. Louis (N.A.E., R.V.P.), the European Union's Horizon 2020 research and innovation program under the Marie Skłodowska-Curie grant MicroREvolution (agreement no. 101023060; T.S.), the Winston Churchill Foundation of the United States (T.J.W.), the Harding Distinguished Post-graduate Scholar Program (T.J.W.), Global Research Technologies Novo Nordisk A/S (H.A., T.P.J.K.), the US National Institutes of Health (R01NS121114 to R.V.P. and R35GM124858 to M.D.L.), the US Air Force Office of Scientific Research (FA9550-20-1-0241 R.V.P.), the European Research Council under the European Union's Seventh Framework Program (FP7/2007–2013) through the ERC grants PhysProt (agreement no. 337969; T.P.J.K.) and the Newman Foundation (T.P.J.K., T.S.).

Author contributions

N.A.E., M.F., T.S., R.V.P. and T.P.J.K. conceived the study. N.A.E., M.F., Y. Q., D.Q., T.S., T. W., T.J.W., H.A., T.J.K., G.C., D.A.W., M.D.L., T.P.J.K. and R.V.P. conducted investigations and interpreted the results. M.D.L., T.P.J.K. and R.V.P. acquired funding. N.A.E., M.F., Y.Q., M.D.L., T.P.J.K., and R.V.P. wrote the original drafts, all authors reviewed and edited the paper.

Competing interests

R.V.P. is a member of the scientific advisory board of and shareholder in Dewpoint Therapeutics Inc. T.P.J.K. is the co-founder of Fluidic Analytics, Wren Therapeutics, Xampla, and Transition Bio. These associations did not influence the work reported here. The remaining authors declare no competing interests and none of the authors have any non-financial interests to declare.

Additional information

Supplementary information The online version contains supplementary material available at <https://doi.org/10.1038/s41467-025-58736-z>.

Correspondence and requests for materials should be addressed to Matthew D. Lew, Tuomas P. J. Knowles or Rohit V. Pappu.

Peer review information *Nature Communications* thanks the anonymous reviewers for their contribution to the peer review of this work. A peer review file is available.

Reprints and permissions information is available at <http://www.nature.com/reprints>

Publisher's note Springer Nature remains neutral with regard to jurisdictional claims in published maps and institutional affiliations.

Open Access This article is licensed under a Creative Commons Attribution-NonCommercial-NoDerivatives 4.0 International License, which permits any non-commercial use, sharing, distribution and reproduction in any medium or format, as long as you give appropriate credit to the original author(s) and the source, provide a link to the Creative Commons licence, and indicate if you modified the licensed material. You do not have permission under this licence to share adapted material derived from this article or parts of it. The images or other third party material in this article are included in the article's Creative Commons licence, unless indicated otherwise in a credit line to the material. If material is not included in the article's Creative Commons licence and your intended use is not permitted by statutory regulation or exceeds the permitted use, you will need to obtain permission directly from the copyright holder. To view a copy of this licence, visit <http://creativecommons.org/licenses/by-nc-nd/4.0/>.

© The Author(s) 2025